2020 IEEE/ASME International Conference on
Advanced Intelligent Mechatronics (AIM), Boston, USA
(Virtual Conference), July 6-9, 2020

A Closed-Loop Controller for a Continuum Surgical Manipulator Based on a Specially Designed Wrist Marker and Stereo Tracking

Haozhe Yang, Baibo Wu, Xu Liu and Kai Xu*, *Member, IEEE*

***Abstract*—Continuum structures have been widely deployed in MIS (Minimally Invasive Surgery) due to its intrinsic dexterity and compliance. However, the absolute tip positioning accuracy of a continuum manipulator may be low compared to a rigid-linked serial manipulator due to its actual bending behaviors that are often different from the assumed ideal ones. Even though the movement accuracy can be improved by motion calibration and actuation compensation, the errors caused by external loads will still exist. In order to improve the tip positioning accuracy of a continuum surgical manipulator, this paper proposes a proof-of-concept approach via integrating a specially designed wrist marker and a closed-loop controller with the visual feedback from a stereo endoscopic camera. The corner detection of the wrist marker was firstly achieved via a modified corner detection algorithm. Then, the tip position was obtained via a pose estimation algorithm that seeks position and orientation of the wrist marker when the corner points in the two images from the stereo endoscopic camera were aligned with the actual corners of the wrist marker. Experimental verification showed that the tip positioning errors were reduced to 25.23% of the original errors during trajectory tracking, demonstrating the effectiveness of the proposed approach.**

I. Introduction

MINIMALLY Invasive Surgery (MIS) has prevailed in recent years due to the reduced invasiveness. But the manipulation challenges during manual MIS triggered the applications of robotic assistance for enhanced accuracy and dexterity to facilitate complex surgical treatments [1].

With robotic presence gradually increased in surgery, continuum surgical robots were found to have great intro-abdominal dexterity and inherent safety [2]. With the segments stacked serially, a continuum surgical manipulator usually has several distal DoFs (Degree of Freedom) for the dexterous manipulation in a patient's body cavity [3-5].

In surgical operations, accurate positioning control is a vital factor. Due to the discrepancy between the assumed ideal bending patterns and the actual bending behaviors with uncertain manufacturing clearance and even under external loads, the absolute positioning accuracy of continuum surgical manipulators can be low. Quite a few methods have been developed to improve the positioning accuracy, including recursive motion calibration [6], backlash hysteresis compensation [7], friction modeling [8], and actuation compensation [4]. Sensing modalities were also integrated to monitor the actual bending shapes, aiming at producing better positioning accuracy. For example, fiber bragg grating (FBG) sensors were used in the continuum manipulator for deflection detection [9]. Electromagnetic (EM) tracking sensors can also be used for shape reconstruction [10].

The integration of FBG or EM sensors requires additional instrumentation. On the other hand, a stereo vision system is often available in a laparoscopic or endoscopic surgical system. Pose information of the end effector can be extracted from the visual feedback from the stereo endoscopic camera, e.g., in [11]. Hence, this paper proposes a proof-of-concept approach via integrating a specially designed wrist marker and a closed-loop controller with the visual feedback from a stereo endoscopic camera, as depicted in Fig. 1.

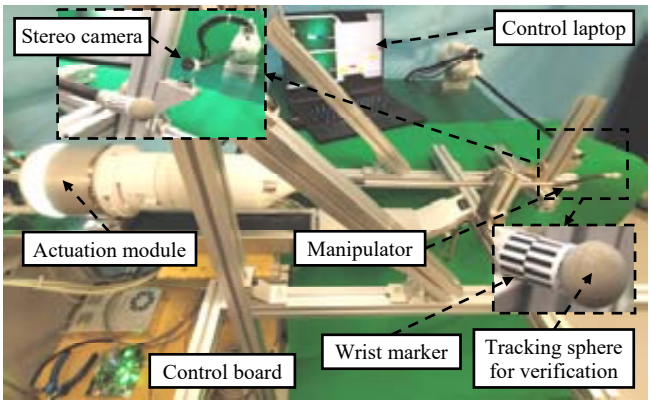

Fig. 1. Setup of the proposed approach of improving tip positioning accuracy for a continuum surgical manipulator via integrating a specially designed wrist marker and a closed-loop controller with the visual feedback from a stereo endoscopic camera.

The pose of the end effector of the surgical continuum manipulator can be obtained from the customized checkerboard-like marker which is attached at the end of the manipulator. After the corner points were detected from the checkerboard-like wrist marker using an algorithm such as in [12, 13], the pose of the surgical end effector can be obtained by solving an optimization problem that minimize the errors between the actual corner points and the expected corner points projected on the right and left imaging planes of the stereo endoscopic camera, since the geometry of the checkerboard-like wrist marker is known. Then the end effector pose information can be used in the proposed closed-loop control scheme to improve the tip positioning accuracy.

Manuscript received on Mar 8th, 2020. This work was supported in part by the National Key R&D Program of China (Grant No. 2017YFC0110800), and in part by the National Natural Science Foundation of China (Grant No. 51722507).

Haozhe Yang, Baibo Wu, Xu Liu and Kai Xu are with School of Mechanical Engineering, Shanghai Jiao Tong University, Shanghai, China (asterisk indicates the corresponding author, phone: +86-21-34206547; e-mails: silence1004@sjtu.edu.cn, wubaibo@sjtu.edu.cn, xu.liu@sjtu.edu.cn and k.xu@sjtu.edu.cn).

The rest of this paper is organized as follows. Section II presents kinematics of the continuum surgical manipulator. The proposed stereo tracking approach, including i) the modified corner detection algorithm, ii) the optimization solving for the tip position, and iii) the closed-loop control formulation, is detailed in Section III. Section IV reports the experimental verification results, while the conclusions and future works are summarized in Section V.

II. Kinematics

In this study, the continuum surgical manipulator is from a previous study in [14], as shown in Fig. 2. It is composed of two serially connected continuum segments (the 1st and 2nd segments) and a base stem. Each segment is a 2-DoF structure. Constant curvature bending assumption [15, 16] is used for the kinematics modeling of the segments. The base stem provides 1-DoF translation and 1-DoF rotation to the segments. In total, the continuum manipulator has 6 DoFs.

The coordinate systems and the nomenclature of the manipulator are defined in Section II.A. The kinematics of a single continuum segment is summarized in Section II.B, while the kinematics of the entire continuum surgical manipulator is derived in Section II.C.

A. Coordinates and Nomenclature

The coordinate systems for the t^{th} segment and for the entire manipulator are showed in Fig. 2(a) and Fig. 2(b), respectively. The nomenclature used in this study is listed in Table I, while the coordinates are detailed as follows.

- World Coordinate System $\{w\}=[\hat{\mathbf{x}}_w \quad \hat{\mathbf{y}}_w \quad \hat{\mathbf{z}}_w]^T$ is attached to the abdominal incision with its Z axis aligned with the base stem.
- The Base Ring Coordinate System of the t^{th} segment $\{tb\}=[\hat{\mathbf{x}}_{tb} \quad \hat{\mathbf{y}}_{tb} \quad \hat{\mathbf{z}}_{tb}]^T$ is attached to the base ring of the t^{th} segment, with the XY plane coinciding with the base ring and the X axis passing through the first backbone.
- Bending Plane Coordinate System 1 of the t^{th} segment $\{t1\}=[\hat{\mathbf{x}}_{t1} \quad \hat{\mathbf{y}}_{t1} \quad \hat{\mathbf{z}}_{t1}]^T$ has its origin coincide with that of $\{tb\}$ and its XY plane coincides with the bending plane of the t^{th} segment.
- Bending Plane Coordinate System 2 of the t^{th} segment $\{t2\}=[\hat{\mathbf{x}}_{t2} \quad \hat{\mathbf{y}}_{t2} \quad \hat{\mathbf{z}}_{t2}]^T$ has its origin located at the center of the end ring of the t^{th} segment and its XY plane aligned with the bending plane of the t^{th} segment.
- End Ring Coordinate System of the t^{th} segment $\{te\}=[\hat{\mathbf{x}}_{te} \quad \hat{\mathbf{y}}_{te} \quad \hat{\mathbf{z}}_{te}]^T$ is attached to the end ring of the t^{th} segment, with the XY plane coinciding with the end ring and its X axis passing through the first backbone.
- Wrist Marker Coordinate System $\{wm\}=[\hat{\mathbf{x}}_{wm} \quad \hat{\mathbf{y}}_{wm} \quad \hat{\mathbf{z}}_{wm}]^T$ has its origin coincide with the center of wrist marker. The X axis passes through one corner.
- Left Lens Coordinate System $\{ll\}=[\hat{\mathbf{x}}_{ll} \quad \hat{\mathbf{y}}_{ll} \quad \hat{\mathbf{z}}_{ll}]^T$ has its origin coincide with the center of the left lens of stereo endoscopic camera. The X axis is oriented to the right lens.
- Right Lens Coordinate System $\{rl\}=[\hat{\mathbf{x}}_{rl} \quad \hat{\mathbf{y}}_{rl} \quad \hat{\mathbf{z}}_{rl}]^T$ has its origin coincide with the center of the right lens of stereo endoscopic camera.

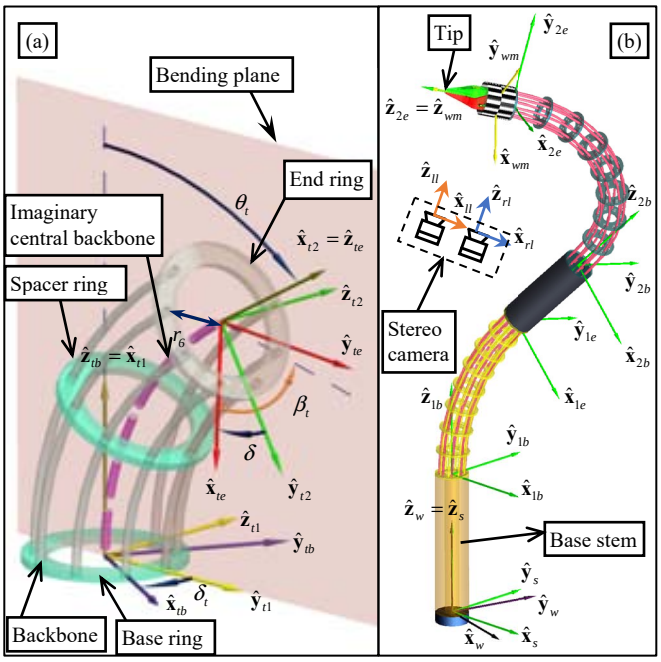

Fig. 2. Nomenclature and coordinates of: (a) the t^{th} continuum segment, and (b) the continuum surgical manipulator from [14].

TABLE I
Nomenclature For the Modeling Kinematics

Symbol	Definition
t	Index of the segments.
L_t	Length of the imaginary central backbone of the t^{th} segment.
θ_t	The angle indicating the rotation from $\hat{\mathbf{x}}_{t1}$ to $\hat{\mathbf{x}}_{t2}$ about $\hat{\mathbf{z}}_{t1}$.
δ_t	The angle from the bending plane to $\hat{\mathbf{x}}_{tb}$ in the t^{th} segment.
φ	Axial rotation angle of the base stem.
d	Feeding length of the base stem.
$\boldsymbol{\psi}_t$	$\boldsymbol{\psi}_t=[\theta_t \quad \delta_t]^T$ is the configuration vector for the t^{th} segment.
$\boldsymbol{\psi}_s$	$\boldsymbol{\psi}_s=[\varphi \quad d]^T$ is the configuration vector for the base stem.
$\boldsymbol{\psi}$	$\boldsymbol{\psi}=[\boldsymbol{\psi}_s^T \quad \boldsymbol{\psi}_1^T \quad \boldsymbol{\psi}_2^T]^T$ is the configuration vector for the continuum manipulator.
${}^a\mathbf{R}_b$	Coordinate transformation matrix from frame $\{b\}$ to frame $\{a\}$.
${}^a\mathbf{p}_b$	Position vector from the origin of the frame $\{a\}$ to the origin of the frame $\{b\}$ in frame $\{a\}$.
$\mathbf{J}_{tv}, \mathbf{J}_{t\omega}$	Jacobian matrices of linear and angular velocities of the t^{th} segment. $\mathbf{v}_t=\mathbf{J}_{tv}\dot{\boldsymbol{\psi}}_t$ and $\boldsymbol{\omega}_t=\mathbf{J}_{t\omega}\dot{\boldsymbol{\psi}}_t$.
l_b^a	The distance between the origin of the frame $\{a\}$ and the origin of the frame $\{b\}$

B. Forward Kinematics of the t^{th} Segment

The kinematics for the t^{th} continuum segment is summarized as follows. The details are in [14, 16].

$$ {}^{tb}\mathbf{p}_{te} = \frac{L_t}{\theta_t}\begin{bmatrix} \cos\delta_t(1-\cos\theta_t) \\ \sin\delta_t(\cos\theta_t - 1) \\ \sin\theta_t \end{bmatrix} \quad (1) $$

$$ {}^{tb}\mathbf{R}_{te} = {}^{tb}\mathbf{R}_{t1}\,{}^{t1}\mathbf{R}_{t2}\,{}^{t2}\mathbf{R}_{te} \quad (2) $$

Where ${}^{tb}\mathbf{p}_{te} = [0 \quad 0 \quad L_t]^T$ when $\theta_t \to 0$.

And the instantaneous kinematics is defined as in Eq. (3).

$$ \dot{\mathbf{x}}_t = \begin{bmatrix} \mathbf{v}_t \\ \boldsymbol{\omega}_t \end{bmatrix} = \mathbf{J}_t\dot{\boldsymbol{\Psi}}_t = \begin{bmatrix} \mathbf{J}_{tv} \\ \mathbf{J}_{t\omega} \end{bmatrix}\begin{bmatrix} \dot{\theta}_t \\ \dot{\delta}_t \end{bmatrix} \quad (3) $$

C. Kinematics of the Manipulator

The kinematics of the 6-DoF continuum manipulator is defined referring to the coordinate systems in Fig. 2(b). The tip position can be expressed in the $\{w\}$ as follows.

$$ {}^{W}\mathbf{p}_{tip} = {}^{W}\mathbf{T}_{1b}\,{}^{1b}\mathbf{T}_{1e}\,{}^{1e}\mathbf{T}_{2b}\,{}^{2b}\mathbf{T}_{2e}\,{}^{2e}\mathbf{p}_{tip} \quad (4) $$

Where ${}^{2e}\mathbf{p}_{tip} = \begin{bmatrix} 0 & 0 & l_{tip}^{2e} \end{bmatrix}^T$ is the tip position expressed in $\{2e\}$.

With the stereo endoscopic camera, the tip position can also be expressed through the coordinate $\{ll\}$.

$$ {}^{W}\mathbf{p}_{tip} = {}^{W}\mathbf{R}_{ll}\left({}^{ll}\mathbf{R}_{wm}\,{}^{wm}\mathbf{p}_{tip} + {}^{ll}\mathbf{p}_{wm}\right) + {}^{W}\mathbf{p}_{ll} \quad (5) $$

Where ${}^{wm}\mathbf{p}_{tip} = \begin{bmatrix} 0 & 0 & l_{tip}^{wm} \end{bmatrix}^T$ is the tip position expressed in the $\{ll\}$. The transformation $[{}^{W}\mathbf{R}_{ll}\ {}^{W}\mathbf{p}_{ll}]$ from $\{W\}$ to $\{ll\}$ is determined by the installation pose of the stereo camera. This info will usually be known if the endoscopic camera is in the same surgical robotic system.

The stereo tracking algorithm in Section III, is used to calculate the transformation $[{}^{ll}\mathbf{R}_{wm}\ {}^{ll}\mathbf{p}_{wm}]$ in real-time.

III. Stereo Tracking Algorithm

The checkerboard-like wrist marker, as shown in Fig. 2(b), is composed of evenly distributed black and white stripes on a cylindrical surface with a diameter of 9.1 mm. The stereo camera is calibrated beforehand with the intrinsic parameters obtained and the lens distortion corrected.

The algorithm proceeds as follows. Firstly, the corners are detected as in Section III.A and Fig. 3(a). Secondly, the transformation $[{}^{ll}\mathbf{R}_{wm}\ {}^{ll}\mathbf{p}_{wm}]$ is estimated to generate the tip position as in Section III.B and Fig. 3(b). Then, a closed-loop controller is implemented to control the manipulator as in Section III.C and Fig. 3(c).

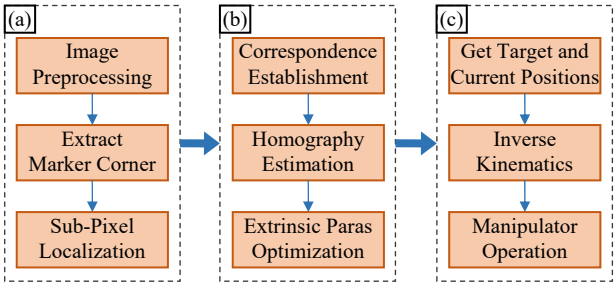

Fig. 3. Major implementation steps of the marker-based stereo tracking and closed-loop control: (a) the corner detection and localization, (b) calculation of the tip position and (c) the closed-loop control algorithm.

A. Marker Corner Detection

The implemented process for corner detection is extended from the corner likelihood method as in [13], combining the template matching technique to increase its robustness. The process is described as follows.

(1) Image preprocessing

Firstly, an image ROI (region of interest) is extracted based on the corners' location clusters of the last frame. The cropped image is then converted to grayscale .

The ROI of the first image is itself.

(2) Extract marker corners

The image ROI is firstly convolved with the Sobel kernel for the first and second derivatives. The responses on each pixel serve as the Corner Likelihood (CL), which is defined as follows:

$$ \begin{aligned} CL &= \max(c_{xy}, c_{45}) \\ c_{xy} &= \varepsilon^2 \cdot \left|I_{xy}\right| - 1.5\cdot\varepsilon\cdot\left(\left|I_{45}\right| + \left|I_{n45}\right|\right) \\ c_{45} &= \varepsilon^2 \cdot \left|I_{45\_45}\right| - 1.5\cdot\varepsilon\cdot\left(\left|I_x\right| + \left|I_y\right|\right) \end{aligned} \quad (6) $$

Where ε is set to 2 as in [13]; I_x, I_{45}, I_y, I_{n45} are the first derivatives in the 0, π/4, π/2, -π/4 directions, respectively; I_{xy} and I_{45_45} are the second derivatives in the 0, π/2 and π/4, -π/4 directions, respectively.

And the orientation I_{angle} and its weight I_{weight} for each pixel can be calculated accordingly.

$$ I_{angle} = \arctan\left(I_y / I_x\right), \quad I_{weight} = \sqrt{I_x^{\,2} + I_y^{\,2}} \quad (7) $$

With the I_{angle} and I_{weight}, two edge orientations for a corner point can be estimated using the mean shift within a 10 ×10 pixel neighborhood.

Non-Maximal Suppression (NMS) in a 5 × 5 pixel neighborhood is applied to localize the points of interest in the ROI. This treatment removes the points when their CLs are less than 0.06. Then, the remaining points are the corner candidates.

The local area of a corner can be described as a hyperbolic tangent model (HTM) with the known edge orientations. To check whether a corner candidate is a marker corner, the correlation coefficient CC between the gray distribution G_{image} in the 10 × 10 rectangular region centered by this candidate corner and the distribution G_{HTM} generated by the HTM is calculated.

$$ CC = \frac{Cov\left(G_{image}, G_{HTM}\right)}{Var\left(G_{image}\right)\cdot Var\left(G_{HTM}\right)} \quad (8) $$

Where *Var* is the variance, while the *Cov* is the covariance.

Based on Eq. (6) to Eq. (8), the corner detection algorithm is proposed. The CL is used to locate the corner at the location of the maximum CL in the 10 × 10 rectangular region. The CC is used to filter the points with their CCs less than 0.8. And the edge orientation can be updated for each detected corner using Eq. (7).

Then, the steps of locating the marker corners are illustrated in Fig. 4. Firstly, the corner candidates are traversed in the order of the CLs until a first marker corner is detected. Then the second marker corner is detected by moving a 10 × 10 rectangular window in the four edge directions. After the first and the second marker corners are

detected, other marker corners are detected consecutively by moving the 10 × 10 windows in the two opposite directions away from the first two detected corners. The process is stopped, when the searched distance is larger than twice of the distance between the previous two found marker corners.

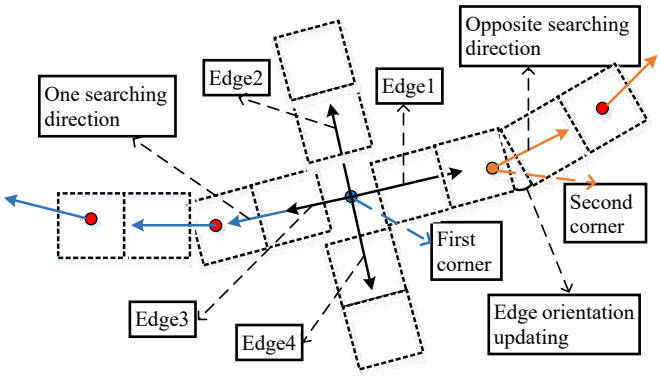

Fig. 4. Steps of the proposed corner detection algorithm

(3) Subpixel localization

A corner can be at a point between the pixels. The problem can be addressed as finding the extremum in a quadric surface of the CLs:

$$S(x,y) = ax^2 + by^2 + cx + dy + exy + f \tag{9}$$

A 7 × 7 neighborhood is used to fit the surface to get the coefficients in Eq. (9). Then, the sub-pixel corner location can be calculated as follows:

$$x_{sub} = \frac{de - 2bc}{4ab - e^2}, y_{sub} = \frac{ce - 2ad}{4ab - e^2} \tag{10}$$

Sub-pixel localization is carried out when a marker corner is detected.

B. Tip Position Optimization

After locating the marker corners in the left and right images of the stereo endoscopic camera, the known 3D dimensions of the wrist marker can be utilized to estimate the manipulator's tip position. The algorithm is described as follows.

(1) Corners correspondence establishment

The captured corners in the left and right images may be different in terms of amount and order. The corners correspondence was established according to the descending y-axis coordinates after the rectification of the endoscopic camera.

Notice that the detected corners are consecutively located on the wrist marker. Therefore, the XY coordinates for the i^{th} marker corner can be written as: $[r_{wm}\cos((i\text{-}1)\beta)\ r_{wm}\sin((i\text{-}1)\beta)]$, where r_{wm} is the wrist marker radius and β is the marker stripe division angle. follows.

Notice that the location of the first detected corner may be different between the two video frames from the stereo camera. So, the coordinate for the i^{th} marker corner is relative in terms of the 1-DOF rolling about the Z axis of $\{wm\}$.

(2) Homography estimation

Homography transformation $\mathbf{H}$ describes the mapping between the model plane and its image plane [12]. For the left lens of the stereo camera, the image point and the 3D point of the i^{th} marker corner are related as follows.

$$^{wm}\tilde{\mathbf{m}}_i = \begin{bmatrix} r_{wm}\cdot\cos\left((i-1)\cdot\beta\right) & r_{wm}\cdot\sin\left((i-1)\cdot\beta\right) & 1 \end{bmatrix}^T \tag{11}$$

$$^{left}s_i \cdot {}^{left}\tilde{\mathbf{m}}_i = \mathbf{H}_{left} \cdot {}^{wm}\tilde{\mathbf{m}}_i \tag{12}$$

$$\mathbf{H}_{left} = \begin{bmatrix} \mathbf{h}_1 & \mathbf{h}_2 & \mathbf{h}_3 \end{bmatrix} = \eta \cdot \mathbf{A} \cdot \begin{bmatrix} \mathbf{r}_1 & \mathbf{r}_2 & {}^{ll}\mathbf{p}_{wm} \end{bmatrix} \tag{13}$$

Where $^{left}\tilde{\mathbf{m}}_i = \begin{bmatrix} u_i & v_i & 1 \end{bmatrix}^T$ is the augmented vector of the i^{th} corner point in the left image; $\mathbf{A}$ is the intrinsic parameter matrix, which is calibrated beforehand; $\mathbf{r_1}$, $\mathbf{r_2}$ are the first two columns of rotation matrix $^{ll}\mathbf{R}_{wm}$; $^{left}s_i$, η are arbitrary non-zero scalars.

Let $\mathbf{x}_H = \begin{bmatrix} \mathbf{h}_1^T & \mathbf{h}_2^T & \mathbf{h}_3^T \end{bmatrix}^T$, the homography matrix can be solved by the following linear equations.

$$\begin{bmatrix} {}^{wm}\tilde{\mathbf{m}}_i^T & \mathbf{0}^T & -u_i \cdot {}^{wm}\tilde{\mathbf{m}}_i^T \\ \mathbf{0}^T & {}^{wm}\tilde{\mathbf{m}}_i^T & -v_i \cdot {}^{wm}\tilde{\mathbf{m}}_i^T \end{bmatrix} \cdot \mathbf{x}_H = \mathbf{0} \Rightarrow \mathbf{L} \cdot \mathbf{x}_H = \mathbf{0} \tag{14}$$

Where $\mathbf{L}$ is a 2n × 9 matrix; n is the number of the detected marker corners.

From Eq. (14), the solution of $\mathbf{x}_H$ is the right singular vector of $\mathbf{L}$ associated with the smallest singular value. With $\mathbf{A}$ and $\mathbf{H}_{left}$ obtained, the extrinsic parameters of the left lens of the stereo camera can be calculated as follows.

$$\mathbf{r}_1 = \kappa \cdot \mathbf{A}^{-1} \cdot \mathbf{h}_1, \mathbf{r}_2 = \kappa \cdot \mathbf{A}^{-1} \cdot \mathbf{h}_2, {}^{ll}\mathbf{p}_{wm} = \kappa \cdot \mathbf{A}^{-1}\mathbf{h}_3 \tag{15}$$

Where $\kappa = 1 / \left\| \mathbf{A}^{-1} \cdot \mathbf{h}_1 \right\| = 1 / \left\| \mathbf{A}^{-1} \cdot \mathbf{h}_2 \right\|$.

(3) Extrinsic parameters optimization

In order to obtain the pose of the wrist marker, the errors between the marker corners on the stereo images and the projected positons on the image planes are minimized with the Levenberg-Marquardt algorithm simultaneously. The results of $[{}^{ll}\mathbf{R}_{wm}\ {}^{ll}\mathbf{p}_{wm}]$ calculated by Eq. (15) are used as the initial guess for this optimization.

$$\min_{[{}^{ll}\mathbf{R}_{wm}\ {}^{ll}\mathbf{p}_{wm}]} \left(\begin{array}{l} \sum_{i=1}^{n} \left(\left\| {}^{left}\tilde{\mathbf{m}}_i - \mathbf{H}_{left} \cdot {}^{wm}\tilde{\mathbf{m}}_i / {}^{left}s_i \right\|^2 \right) + \\ \sum_{i=1}^{n} \left(\left\| {}^{right}\tilde{\mathbf{m}}_i - \mathbf{H}_{right} \cdot {}^{wm}\tilde{\mathbf{m}}_i / {}^{right}s_i \right\|^2 \right) \end{array} \right) \tag{16}$$

Where $\mathbf{H}_{left}$, $\mathbf{H}_{right}$ are the homography matrices of the left and right lens of the stereo camera, respectively; $\mathbf{H}_{right}$ can be expressed by $\mathbf{H}_{left}$ with the distance l_{rl}^{ll} between the center of the two lens.

C. Closed-Loop Control Algorithm

The proposed closed-loop control algorithm can improve the tip positioning accuracy using the visual feedback from the stereo camera. The flowchart of the closed-loop controller is shown in Fig. 5.

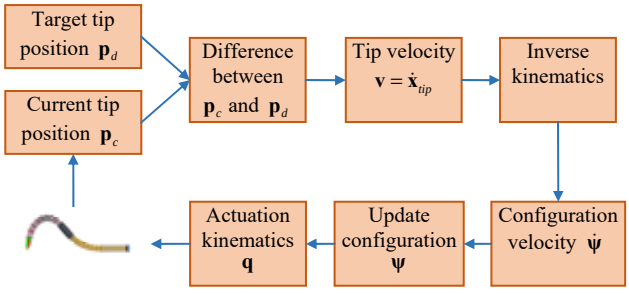

Fig. 5. Flowchart of the closed-loop control of the continuum manipulator.

The target tip position $\mathbf{p}_d$ from the surgeon's input device is periodically transferred into closed-loop controller. Current tip position $\mathbf{p}_c = {}^W\mathbf{p}_{tip}$ is the feedback obtained from the stereo endoscopic camera. The difference between $\mathbf{p}_d$ and $\mathbf{p}_c$ is calculated as in Eq. (17).

$$\Delta\mathbf{p} = \mathbf{p}_d - \mathbf{p}_c \tag{17}$$

The tip linear velocity $\mathbf{v}$ and the configuration velocity $\dot{\boldsymbol{\psi}}$ can be obtained as in Eq. (18) and Eq. (19) respectively.

$$\mathbf{v} = v_{\mathrm{xlim}}\Delta\mathbf{p} / \left\|\Delta\mathbf{p}\right\| \tag{18}$$

$$\dot{\boldsymbol{\psi}} = \mathbf{J}^{+}\begin{bmatrix}\mathbf{v}^T & \boldsymbol{\omega}^T\end{bmatrix}^T \tag{19}$$

Where v_{xlim} is a constant for a maximally allowed linear velocity; $\mathbf{J}^{+}$ is the Moore–Penrose pseudoinverse inverse matrix of $\mathbf{J}$, which can be improved by a singularity robust formulation as in Eq. (20).

$$\mathbf{J}^{+} = \mathbf{J}^T\left(\mathbf{J}\mathbf{J}^T + \gamma\mathbf{I}\right)^{-1}, \sigma_{\min} < \xi \tag{20}$$

Where $\sigma_{\min}$ is the smallest non-zero singular value; γ and ξ are preset small positive numbers.

The configuration vector is updated as in Eq. (21).

$$\boldsymbol{\psi} = \boldsymbol{\psi} + \dot{\boldsymbol{\psi}}\Delta t \tag{21}$$

Where Δt is the servo loop cycle.

In the next servo loop, after moving the manipulator for a small step, the stereo camera captures images again and a new $\mathbf{p}_c$ is obtained for the closed-loop controller.

IV. Experimental Verifications

To evaluate the effectiveness of the proposed stereo tracking algorithm and the closed-loop controller, several experiments have been conducted with the experimental setup shown in Fig. 6. The accuracy of the tip position is verified as in Section IV.B. The closed-loop control experiment was compared with the open-loop control one in Section IV.C.

A. Experimental Setup

The continuum surgical manipulator is driven by a actuation module as in Fig. 1. The actuation module can translate the base stem of the manipulator along the z-axis as well as rotate it around the z-axis. It also actuates the bending motions of the two segments.

The stereo endoscopic camera is located at the distal portion of a vision manipulator. In this preliminary experimental verification, it was fixed at a location such that the view of the surgical manipulator is similar in size to that during a surgical operation. The stereo camera has two HD chips with a resolution of 1920×1080. Under this setup, the transformation $[{}^W\mathbf{R}_{ll}\ {}^W\mathbf{p}_{ll}]$ from $\{W\}$ to $\{ll\}$ is constant during the experiments.

The Polaris Vega optical tracker (Northern Digital, Inc) and a sphere marker were used to get the ground truth of the tip position of the surgical manipulator. The tracker has a volumetric accuracy of 0.12mm RMS.

The wrist marker is attached on the distal portion of the manipulator as shown in Fig. 6.The center was 15 mm from the tip location, where the sphere marker for the optical tracker is fixed.

The control program implemented in C++ runs on a laptop with an Intel i7-9750H 2.60GHz CPU. The average time spent on the image processing, including the stereo images acquisition, corners detection and tip position calculation, is about 45ms. The control cycle should be larger than the feedback period, thus setting to 60ms.

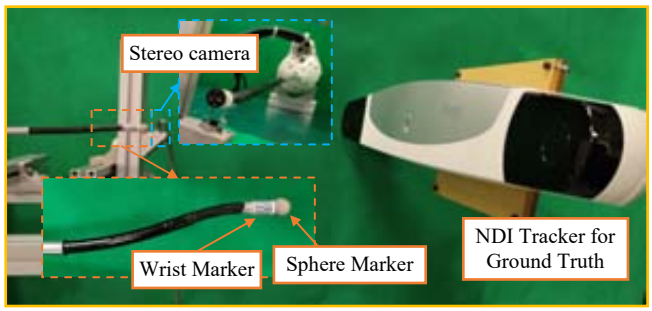

Fig. 6. Experimental setup: the wrist marker and the sphere marker. The wrist marker is captured by the fixed stereo camera for calculating the tip position, while the center of the sphere marker is regarded as the ground truth for the experiments.

B. Tip Position Accuracy

The accuracy of the tip position obtained from the stereo tracking algorithm, is determined during the following pose following experiments.

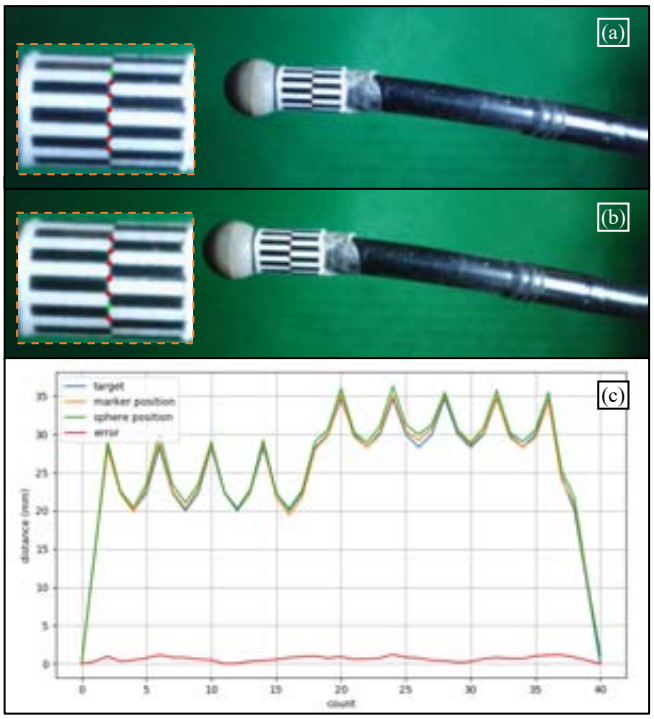

Fig. 7. Experiment for the tip positioning accuracy: (a) the image from left lens with detected corners, (b) the image from the right one, and (c) comparison between the detected tip position and the ground truth.

Figure 7(a) shows the image from left lens, while Fig. 7(b) shows one from the right one. Corners with sub-pixel localization are plotted as well. The sphere marker was tracked by the NDI tracker for ground truth of the tip position. The tip of the manipulator was moved to the 40 positions within the workspace. Each movement has an incremental distance as shown in Fig. 7(c).The distance errors are also plotted.

For the given movement targets, The average error is 0.67 mm, while the maximal error is 1.21 mm.

C. Closed-Loop Control Experiments

The inclusion of the closed-loop control for manipulator enables accurate trajectory tracking without modeling the unknown and changing friction and backlashes that affect the tip positioning accuracy. To demonstrate the improvement after the proposed closed-loop control, an open-loop control was also performed for comparison.

Using both the closed-loop control and the open-loop control, the manipulator tip was moved along the edges of a cube of 20 mm by 40 mm and 40 mm within the workspace. Please note that the camera was about 80 mm away from the manipulator tip, the edge length of the trajectory cube is limited to the image size. The tip following velocity was set to 10 mm/s in both experiments.

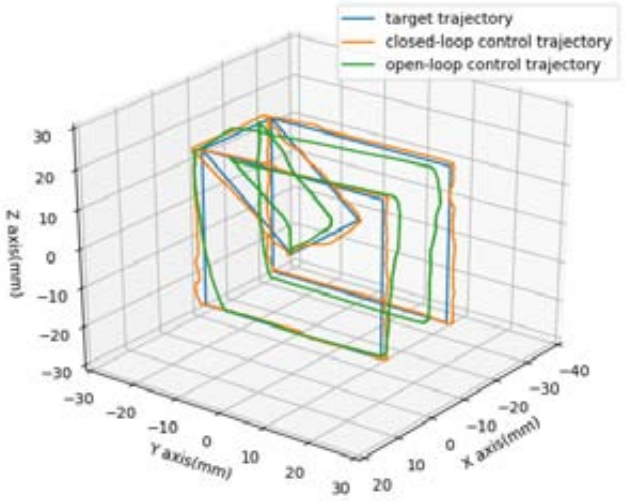

Fig. 8. Experiment for comparing the closed-loop and the open-loop controllers.

The results are shown in Fig. 8. Compared with the open-loop control, the closed-loop control reduces the average error from 3.25 mm to 0.82 mm and the maximal error from 8.40 mm to 2.59 mm.

There existed overshoots when the manipulator changes motion direction. The main reason may be that the control cycle is a bit longer than the preferred. This can be further improved when the algorithm is refined.

V. Conclusions and Future Work

In this paper, a closed-loop controller based on a specially designed wrist marker and stereo tracking is proposed to improve the tip positioning accuracy of a continuum surgical manipulator. A checkerboard-like wrist marker is attached at the end of the manipulator and viewed by the stereo endoscopic camera. After the corner points are detected from the two images. The marker position is obtained through a pose estimation algorithm utilizing the detected marker corner positions and the known marker dimensions.

Then, a closed-loop control is put forward to move the manipulator with the feedback from the stereo endoscopic camera. The experiments shown that the trajectory tracking errors can be reduced to 25.23% of the errors generated under the open-loop control, demonstrating the efficacy.

Future works mainly include three aspects: i) further verify the proposed approach under different loading conditions, ii) refine the algorithm implementation for quick control cycles, and iii) re-design the wrist marker in terms of color and pattern such that the end effector rolling DoF can be obtained.

References

[1] R. H. Taylor, "A Perspective on Medical Robotics," *Proceedings of the IEEE,* Vol. 94, No.9, pp. 1652- 1664, 2006.

[2] J. Burgner-Kahrs, D. C. Rucker, and H. Choset, "Continuum Robots for Medical Applications: A Survey," *IEEE Transactions on Robotics,* Vol. 31, No.6, pp. 1261-1280, Dec 2015.

[3] P. E. Dupont, J. Lock, B. Itkowitz, and E. Butler, "Design and Control of Concentric-Tube Robots," *IEEE Transactions on Robotics,* Vol. 26, No.2, pp. 209-225, April 2010.

[4] K. Xu, J. Zhao, and M. Fu, "Development of the SJTU Unfoldable Robotic System (SURS) for Single Port Laparoscopy," *IEEE/ASME Transactions on Mechatronics,* Vol. 20, No.5, pp. 2133-2145, Oct 2015.

[5] J. Shang, K. Leibrandt, P. Giataganas, V. Vitiello, C. A. Seneci, P. Wisanuvej, J. Liu, G. Gras, J. Clark, A. Darzi, and G.-Z. Yang, "A Single-Port Robotic System for Transanal Microsurgery - Design and Validation," *IEEE Robotics and Automation Letters,* Vol. 2, No.3, pp. 1510-1517, July 2017.

[6] K. Xu and N. Simaan, "Actuation Compensation for Flexible Surgical Snake-like Robots with Redundant Remote Actuation," in *IEEE International Conference on Robotics and Automation (ICRA)*, Orlando, Florida, USA, 2006, pp. 4148- 4154.

[7] N. Simaan, K. Xu, A. Kapoor, W. Wei, P. Kazanzides, P. Flint, and R. H. Taylor, "Design and Integration of a Telerobotic System for Minimally Invasive Surgery of the Throat " *International Journal of Robotics Research,* Vol. 28, No.9, pp. 1134-1153, 2009.

[8] T. N. Do, T. Tjahjowidodo, M. W. S. Lau, and S. J. Phee, "Nonlinear Friction Modelling and Compensation Control of Hysteresis Phenomena for a Pair of Tendon-Sheath Actuated Surgical Robots," *Mechanical Systems and Signal Processing,* Vol. 60, No.61, pp. 770-784, 2015.

[9] B. Kim, J. Ha, F. C. Park, and P. E. Dupont, "Optimizing Curvature Sensor Placement for Fast, Accurate Shape Sensing of Continuum Robots," in *IEEE International Conference on Robotics and Automation (ICRA)*, Hong Kong, China, 2014, pp. 5374-5379.

[10] L. Wu, S. Song, K. Wu, C. M. Lim, and H. Ren, "Development of a Compact Continuum Tubular Robotic System for Nasopharyngeal Biopsy," *Medical & Biological Engineering & Computing,* Vol. 55, No.3, pp. 403-417, 2017.

[11] X. Ma, C. Song, P. W. Chiu, and Z. Li, "Autonomous Flexible Endoscope for Minimally Invasive Surgery With Enhanced Safety," *IEEE Robotics and Automation Letters,* Vol. 4, No.3, pp. 2607-2613, 2019.

[12] Z. Zhang, "Flexible Camera Calibration by Viewing a Plane from Unknown Orientations," in *IEEE International Conference on Computer Vision (ICCV)*, Kerkyra, 1999, pp. 666-673.

[13] A. Geiger, F. Moosmann, Ö. Car, and B. Schuster, "Automatic Camera and Range Sensor Calibration Using a Single Shot," in *IEEE International Conference on Robotics and Automation (ICRA)*, Saint Paul, Minnesota, USA, 2012, pp. 3936-3943.

[14] S. a. Zhang, Y. Chen, Q. Li, B. Zhao, and K. Xu, "Kinematic Optimization of a Continuum Surgical Manipulator," in *IEEE International Conference on Robotics and Biomimetics (ROBIO)*, Kuala Lumpur, Malaysia, 2018, pp. 2069-2074.

[15] R. J. Webster and B. A. Jones, "Design and Kinematic Modeling of Constant Curvature Continuum Robots: A Review " *International Journal of Robotics Research,* Vol. 29, No.13, pp. 1661-1683, Nov 2010.

[16] K. Xu and N. Simaan, "Analytic Formulation for the Kinematics, Statics and Shape Restoration of Multibackbone Continuum Robots via Elliptic Integrals," *Journal of Mechanisms and Robotics,* Vol. 2, No.011006, pp. 1-13, Feb 2010.